Wiley Analytical Science

The Current State of Reconstruction Technologies for 3D X-ray Microscopy including Algorithmic Innovation for AI-based Recovery

April 26, 10:00am - 11:00am EDT

Many properties can only be fully understood in 3D, such as porosity and tortuosity in porous materials, network connection maps in neuroscience, or mechanical properties in 3D additively manufactured structures. X-ray microscopy provides a unique method to image samples non-destructively in 3D across a wide range of materials and life sciences.

Watch this session during the WAS Virtual Conference:

Nicolas Guenichault, Ph.D.   **Dr. Stephen T. Kelly, Ph.D.**

Register Now

This talk is sponsored by **ZEISS**

Highly Improved Photocurrent Density and Efficiency of Perovskite Solar Cells via Inclined Fluorine Sputtering Process

Eunmi Cho, Jung Geon Son, Chan Beom Park, In Kim, Dohun Yuk, Jin-Seong Park, Jin Young Kim,* and Sang-Jin Lee*

Increase in incident light and surface modification of the charge transport layer are powerful routes to achieve high-performance efficiency of perovskite solar cells (PSCs) by improving the short-circuit current density (J_{SC}) and charge transport characteristics, respectively. However, few techniques are studied to reduce reflection loss and simultaneously improve the electrical performance of the electron transport layer (ETL). Herein, an inclined fluorine (F) sputtering process to fabricate high-performance PSCs is proposed. The proposed process simultaneously implements the antireflection effect of F coating and the effect of F doping on a TiO$_2$ ETL, which increases the amount of light transmitted into the PSC due to the extremely low refractive index ($\approx$1.39) and drastically improves the electrical properties of TiO$_2$. Consequently, the J_{SC} of the F coating and doping perovskite solar cell (F-PSC) increased from 25.05 to 26.01 mA cm^{-2}, and the power conversion efficiency increased from 24.17% to 25.30%. The unencapsulated F-PSC exhibits enhanced air stability after 900 h of exposure to ambient environment atmosphere (30% relative humidity, 25 °C under dark condition). The inclined F sputtering process in this study can become a universal method for PSCs from the development stage to commercialization in the future.

1. Introduction

Owing to the extensive use of non-renewable fossil fuels and the subsequent catastrophic destruction caused to the environment, the development of technologies for utilizing renewable and clean energy sources such as the solar energy has become urgent. Perovskite solar cells (PSCs) are rapidly emerging as one of the most promising photovoltaic technologies owing to their high power conversion efficiency (PCE), easy manufacturing protocol, and low-cost fabrication processing.[1–6] Researchers are increasingly focusing on the development of high-performance PSCs so that they can be successfully commercialized, and many strategies to increase the PCE of PSCs have been reported over the past decade.[7–12]

Jeong et al. used a pseudo-halide anion formate to suppress the defects on the surface of α-FA-based lead triiodide (α-FAPbI$_3$) and increase the crystallinity, affording a high PCE of 25.6%.[13] Kim et al. recently reported that lithium-doped mesoscopic TiO$_2$ can improve the electrical properties of mesoporous TiO$_2$ to afford a high current density of over 26 mA cm^{-2} and PCE of 25.3%.[14] In addition, Min et al. designed a defect-minimized interface between a SnO$_2$ electron transport layer (ETL) and perovskite, achieving a PCE of 25.5% (certified) that was attributable to the enhanced charge extraction and transport.[15] In another study, Kim et al. reported a (polyacrylic acid (PAA)–quantum dot (QD)–SnO$_2$ @compact-TiO$_2$ (c-TiO$_2$)) structure in which PAA-QD-SnO$_2$ was deposited on c-TiO$_2$. The light absorption in this structure was significantly improved with a perovskite layer, achieving a short-circuit current density (J_{SC}) of 26.4 mA cm^{-2}.[16] To date, strategies to fabricate high-performance PSCs have focused on perovskite materials, charge transport materials (to reduce carrier loss), and photon management (to improve J_{SC}).[17–20]

Fluorine (F), the most electronegative element (electronegativity = 4.0), can significantly alter the energy level of materials; consequently, the performance and stability of PSCs can be improved using F.[21–25] Because of the small atomic radius of F (120 pm; van der Waals radius is 147 pm, which is close to that of the hydrogen atom), fluorination of materials does not affect molecular packing.[26,27] Moreover, F has low polarizability because of the strong interaction between the electrons and

E. Cho, I. Kim, S.-J. Lee
Chemical Materials Solutions Center
Korea Research Institute of Chemical Technology (KRICT)
Daejeon 34114, Republic of Korea
E-mail: leesj@krict.re.kr

E. Cho, J.-S. Park
Department of Materials Science and Engineering
Hanyang University
Seoul 04763, Republic of Korea

J. G. Son, C. B. Park, D. Yuk, J. Y. Kim
School of Energy and Chemical Engineering
Ulsan National Institute of Science and Technology (UNIST)
Ulsan 44919, Republic of Korea
E-mail: jykim@unist.ac.kr

J. Y. Kim
Graduate School of Carbon Neutrality
Ulsan National Institute of Science and Technology (UNIST)
Ulsan 44919, Republic of Korea

The ORCID identification number(s) for the author(s) of this article can be found under https://doi.org/10.1002/adfm.202301033.

nucleus. Consequently, F-based polymers have low refractive indices and low dielectric constants.[22,28] Owing to the strong C—F bond, fluorinated compounds exhibit higher thermal and oxidative stabilities,[29–31] thereby rendering fluorinated materials suitable for application in PSCs. Zhu et al. used the 1,3-dimethyl-3-imidazolium hexafluorophosphate (DMIMPF$_6$) ionic liquid (IL) containing F to modify the perovskite surface. The DMIMPF$_6$ IL easily passivated the perovskite surface through electrostatic interactions between Pb^{2+} ions and DMIMPF$_6$, affording a high efficiency of 23.3%.[32] Zhu et al. reported that the doping of a TiO$_2$ ETL with ammonium fluoride (NH$_4$F) improved the electrical properties of the ETL of the PSC. The NH$_4$F-treated TiO$_2$ exhibited a more uniform morphology, reduced carrier recombination, and improved electron extraction from the perovskite, resulting in a significant increase in the PCE from 18.6% to 20.5%.[33] Yoo et al. combined an antireflection coating (ARC) of MgF$_2$, a low-refractive-index material, with a moth-eye structure to reduce reflection loss in the visible region. As a result, J_{SC} of the PSC increased by 11.80% and the PCE increased from 18.2% to 20.5%.[34] Overall, fluorination can significantly improve PSC performance by improving the surface morphology, charge transport properties, and optical properties. However, to date fluorination has yet to achieve high photovoltaic performance.

In this paper, we propose a method for improving J_{SC} and PCE of PSCs by applying an ARC of F and harnessing the F doping effect on the ETL using an inclined F sputtering process at the same time. The F coating was fabricated by a sputtering process using perfluoroalkoxy alkane (PFA) targets with the lowest refractive index (1.34) among polymers. The F coating forms bonds at high F contents, such as C—F$_3$ and C—F$_2$, which result in a low refractive index owing to the low polarizability of F atoms. The antireflection (AR) F coating can reduce reflection losses and increase the amount of light transmitted into the PSC, thereby leading to an increase in J_{SC}. In addition, inclined dual sputtering was employed such that F could be doped into the backside of the TiO$_2$ ETL. Owing to the high electronegativity and small atomic size of F, the electrical properties of the F-doped TiO$_2$ (F-TiO$_2$) ETL were significantly improved, increasing by 45% compared to the initial value. Consequently, the J_{SC} of the F coating and doping perovskite solar cell (F-PSC) increased from 25.05 to 26.01 mA cm^{-2}, and the PCE increased from 24.17% to 25.30%. Thus, the inclined F sputtering process is a concise but high-impact method to improve the efficiency of PSCs by simultaneously implementing AR and F doping effects on the ETL.

2. Results and Discussion

2.1. Antireflection Effect by F Coating

Figure 1 shows the schematic of the fabrication process and the chemical and optical properties of the AR F coatings. During the sputtering of carbon nanotube (CNT)-PFA composite targets, C and F atoms (or molecules) were randomly deposited on the substrate through decomposition and recombination processes (Figure 1a). Figure 1b shows the cross-sectional transmission electron microscopy (TEM) images of the F coating. The

sputtered F coating with nanometer-scale thickness was deposited on the substrate. Elemental mapping confirmed the uniform distribution of F throughout the F coating. Atomic force microscopy (AFM) images (Figure S1, Supporting Information) indicated a smooth surface (Ra = 0.521 nm) of the F coating. Figure 1c shows the F 1s and C 1s X-ray photoelectron spectroscopy (XPS) profiles. PFA exhibits two peaks corresponding to the C—F$_3$ (294.0 eV) and C—F$_2$ (292.0 eV) bonds. The F coating exhibits overlapping peaks originating from the C—F (290.0 eV), C—CF$_n$ (287.4 eV), and C—(C,H) (285.4 eV) bonds, in addition to the aforementioned peaks at 294.0 and 292.0 eV. Because of the low surface energies of C—F$_3$ (6 mN m^{-1}) and C—F$_2$ (18.5 mN m^{-1}), the F coating has a water contact angle (WCA) of 108°, similar to that of PFA, indicating a hydrophobic surface.[35] Additionally, as shown in the spectroscopic ellipsometry (SE) results (Figure 1d), the F coating has a refractive index of 1.39 at 550 nm and exhibits a low refractive index over a wide wavelength range.

Figure 1e and **Table 1** show the optical properties of F-doped tin oxide (FTO), TiO$_2$ coated on FTO (FTO/TiO$_2$), and the F coating deposited on the glass/FTO/TiO$_2$ (F coating/FTO/TiO$_2$) substrate, respectively. After TiO$_2$ was coated on the FTO glass, the average transmittance in the visible region decreased significantly from 78.2% to 72.6%. This is because when light travels from glass to FTO and TiO$_2$, which have high refractive indices, light is reflected multiple times at the interface due to internal reflection, thereby decreasing the total amount of transmitted light. As a result, a reduced amount of incident light reaches the perovskite layer. However, after the AR F coating was applied, the average transmittance drastically increased by 3.2% (from 72.6% to 75.8%) at the optimized thickness.

According to the Fresnel equations, when the F coating was deposited on the glass substrate, the reflection coefficient was 0.027 for the light traveling from air ($n = 1$) to the F coating ($n \approx 1.39$). This is an ≈36% decrease in the reflection coefficient of 0.042 that occurs when light is incident directly from air ($n = 1$) to glass ($n \approx 1.52$). Thus, the reflection decreased owing to refractive index mismatch. In conclusion, the F coating deposited on the glass surface significantly increased the amount of light incident through the glass, and accordingly, the amount of light passing through the film with a high refractive index increased. As shown in the inset of Figure 1e, the reflection from F coating/FTO/TiO$_2$ was reduced in relation to that from FTO/TiO$_2$, and the text could be seen more clearly beyond the substrate. In Figure S2 (Supporting Information), the average transmittance of the F coating/FTO/TiO$_2$ substrate as a function of the F coating thickness increased from 72.6% to 74.6% in the visible range, and the average reflectance decreased from 6.6% to 5.0% under all thickness values. The average reflectance decreased by 24% compared to that of FTO/TiO$_2$.

Figure 1f shows the average transmittance from the FTO glass, FTO/TiO$_2$, and F coating/FTO/TiO$_2$ in the visible range; the figure of merit (FoM) values are summarized in Table 1. The FoM is an index for evaluating the performance of transparent conductive electrodes that are used in PSCs, display devices, and other similar applications. In the present study, Haacke's FoM was calculated from the measured electrical and optical parameters using Equation 1.[36–38]
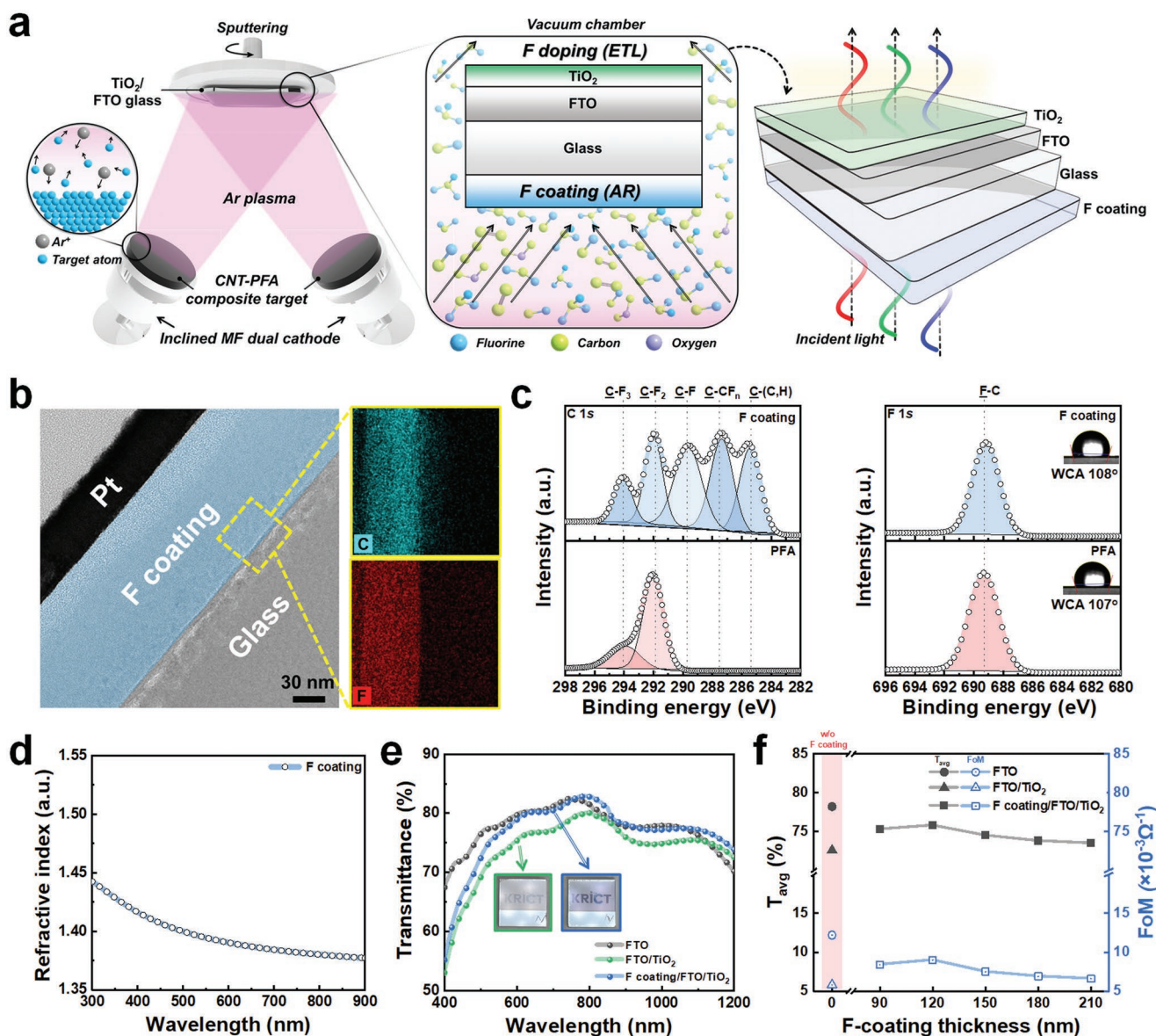
2301033 (2 of 11)

Figure 1. Antireflection effect upon F coating. a) Schematic of the F coating by the inclined fluorine sputtering process. b) Cross-sectional TEM image of the F coating on glass and element mapping images. c) C 1s and F 1s XPS spectra of the F coating and PFA (inset shows the WCA of PFA and F coating). d) Correlation between the refractive index and wavelength of F coating. e) Transmittance spectra of FTO, FTO/TiO$_2$, and F coating/FTO/TiO$_2$ in the wavelength range of 400–1200 nm (inset: photographs of the FTO/TiO$_2$ and F coating/FTO/TiO$_2$). f) Average transmittance (T$_{avg}$ (400–800 nm), black) and FoM (blue) spectra of F coating/FTO/TiO$_2$ as a function of the F coating thickness.

Table 1. Optical and electrical properties and FoM of F coating/FTO/TiO$_2$ as a function of F coating thickness.

		T$_{avg}$ [%]		R$_{sh}$ [Ω sq^{-1}]	FoM [×10^{-3} Ω^{-1}]	
		@400–800 nm	@400–1200 nm		@400–800 nm	@400–1200 nm
FTO on glass		78.2	77.6	7.0	12.2	11.3
F coating/FTO/TiO$_2$	0 nm	72.6	74.2	7.0	5.8	7.2
	90 nm	75.3	76.4	7.0	8.4	9.7
	120 nm	75.8	76.8	7.0	9.0	10.2
	150 nm	74.5	76.2	7.0	7.5	9.4
	180 nm	73.8	75.5	7.0	6.9	8.6
	210 nm	73.5	75.8	7.0	6.6	8.9

**ADVANCED
SCIENCE NEWS**

www.advancedsciencenews.com

**ADVANCED
FUNCTIONAL
MATERIALS**

www.afm-journal.de

$$\text{FoM} = \frac{T_{\text{avg}}^{10}}{R_{\text{sh}}} \tag{1}$$

where T_{avg} is the average transmittance obtained in the visible wavelength range of 400–800 nm and R_{sh} is the sheet resistance.

When TiO$_2$ was coated on the FTO glass, the FoM value of the substrate decreased drastically from 12.2×10^{-3} to 5.8×10^{-3} Ω^{-1} owing to the decrease in transmittance. When the F coating was deposited on this substrate, the sheet resistance remained unchanged (7 Ω sq^{-1}), while the transmittance increased owing to the antireflection effect. Thus, the FoM and average transmittance increased with a similar trend. For a 120 nm-thick F coating, the average transmittance increased the maximum in the visible range, with the highest FoM value of 9.0×10^{-3} Ω^{-1}. Thus, when the F coating with a low refractive index is applied to the TiO$_2$ ETL coated on FTO, the FoM value and transmittance increase significantly.

2.2. F-Doped TiO$_2$ Electron Transporting Layer

Figure 2 shows the changes in the chemical and physical properties of the TiO$_2$ ETL after F coating. The F coating was fabricated using an inclined dual-sputtering method, wherein power was applied simultaneously to the dual cathode using a mid-range frequency (MF) power supply, which is advantageous for high process efficiency and large-area coating. As shown in Figure 1a, the dual-sputtering cathodes were inclined at an angle of ≈10° to ensure uniform F coating and to ensure that the F plasma reaches both front and back sides of the substrate. The TEM image and elemental mapping (Figure 2a) confirmed the uniform distribution of F on TiO$_2$. F-doped TiO$_2$ was labeled F-TiO$_2$ (F coating thickness was 120 nm, at which the AR effect was maximum). Time-of-flight secondary ion mass spectrometry (TOF-SIMS) (Figure 2b; Figure S3, Supporting Information) revealed a higher F content on the F-TiO$_2$ surface than on the TiO$_2$ surface.

Next, the F 1s and O 1s XPS spectra (Figure 2c and Figure 2d) were acquired to investigate the change in the chemical
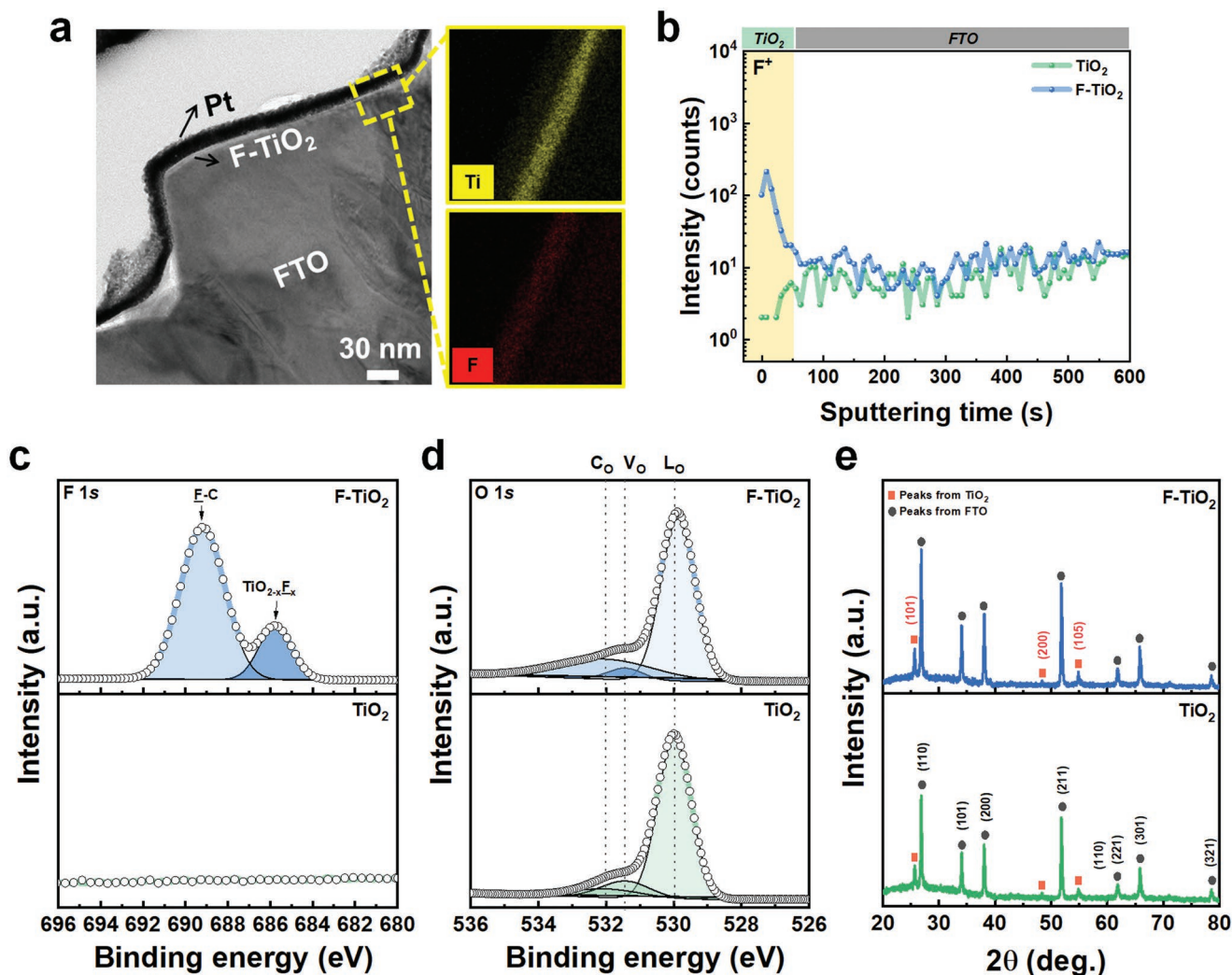

Figure 2. Impact of F doping in TiO$_2$ with and without the F coating. a) Cross-sectional TEM image and element mapping of F-TiO$_2$. b) Elemental depth profiles of TiO$_2$ and F-TiO$_2$ obtained by TOF-SIMS. c) F 1s and d) O 1s XPS spectra of TiO$_2$ and F-TiO$_2$. e) XRD patterns of TiO$_2$ and F-TiO$_2$.

**ADVANCED
SCIENCE NEWS**

www.advancedsciencenews.com

**ADVANCED
FUNCTIONAL
MATERIALS**

www.afm-journal.de

Table 2. Chemical composition of the TiO$_2$ and F-TiO$_2$ layer.

Element [at.%]	TiO$_2$	F-TiO$_2$
O 1s	50.1	38.7
Ti 2p	23.7	19.2
C 1s	26.2	31.5
F 1s	–	10.6

structure of TiO$_2$ and F-TiO$_2$. No peak corresponding to F atom is observed for the TiO$_2$ spectrum (Figure 2c, bottom panel), while two peaks at binding energies of 689.2 and 685.8 eV, corresponding to F—C and TiO$_{2-x}$—F$_x$, respectively, are observed for F—TiO$_2$ (Figure 2c, top panel).[39] Figure S4 (Supporting Information) shows the survey spectra of TiO$_2$ and F-TiO$_2$, and **Table 2** lists the concentration of each atom (O 1s, Ti 2p, C 1s, and F 1s atoms). The atomic concentration of F 1s increases from 0 to 10.6 at.%. Because F is more electronegative than oxygen (F = 4.0, O = 3.44), the former can occupy an oxygen vacancy (V_O) site in the TiO$_2$ structure [40] and form a Ti—F bond (bond energy = 581 kJ mol^{-1}), which is stronger than the Ti—O bond (bond energy = 478 kJ mol^{-1}).[41] Figure 2d shows the O 1s XPS spectra of TiO$_2$ and F-TiO$_2$. To investigate the V_O in the TiO$_2$ structure, the O 1s XPS spectra were fitted with three Gaussian curves centered at binding energies of 530.0, 531.4, and 532.4 eV, corresponding to lattice oxygen (L_O), oxygen vacancy or defect (V_O), and chemisorbed oxygen species (C_O), respectively. The low binding energy peak (L_O) originates from the lattice oxygen atoms (O^{-2}) in a structure in which TiO$_2$ is fully coordinated with Ti^{+4} ions, mainly in the bulk. The medium binding energy peak (V_O) is attributed to the oxygen (O$^-$, O^{-2}) vacancy of the metal oxide. The high binding energy peak (C_O) is attributed to organic contaminants on the surface, which can be significantly reduced by ultraviolet/ozone (UVO) treatment (Table S1 and Figure S5, Supporting Information).[42,43] When TiO$_2$ was doped with F atoms, the peak area of V_O decreased from 12.0% to 5.2% (Table S1, Supporting Information). Therefore, the XPS results clearly confirm the reduction in V_O density of F-TiO$_2$ due to the introduction of F atoms.

Figure 2e and Figure S6 (Supporting Information) show the X-ray diffraction (XRD) patterns of TiO$_2$ and F-TiO$_2$. The characteristic diffraction peak of the (101) plane of anatase TiO$_2$ was observed at 26.84° for both the samples.[44] Even after F doping, the peak did not shift, indicating that F effectively occupied the V_O sites. The average crystallite size of TiO$_2$, as calculated from the (101) diffraction peak of anatase using the Debye–Scherrer equation, also did not change after F doping (Table S2, Supporting Information). This is because the similar ionic radii of F (1.36 Å) and oxygen (1.40 Å) effectively reduce the lattice distortion in relation to that resulting from metal-cation doping.[40,45]

2.3. Enhanced Charge Transport Properties of the F-TiO$_2$ Layer

Figure 3a shows the energy level diagrams of the perovskite devices. To analyze the effect of F doping on TiO$_2$, ultraviolet photoemission spectroscopy (UPS) was conducted (Figure S7, Supporting Information). The Fermi level (E_F) was calculated as

$-(h\nu - E_{cut-off})$, where $h\nu$ (= 21.22 eV) is the energy of the ultraviolet photon source and $E_{cut-off}$ is the secondary electron cutoff of the highest binding energy. The highest occupied molecular orbital (HOMO) energy was calculated from the cutoff value of the lowest binding energy. Figure S8 (Supporting Information) shows the absorption spectra and Tauc plots of pristine TiO$_2$ and F-TiO$_2$ deposited on the FTO/glass substrates. The bandgaps of TiO$_2$, as determined from the intersection of the baseline and dotted line in the Tauc plots, were same (3.57 eV) regardless of F doping. The lowest unoccupied molecular orbital (LUMO) energy was calculated from the difference between the HOMO energy and bandgap. According to the above results, E_F, HOMO energy and LUMO energy for pristine and F-TiO$_2$ are shown in Table S3 (Supporting Information). The difference between E_F and the intrinsic energy level (E_i) is lower for F-TiO$_2$ (0.62 eV) than for pristine TiO$_2$ (0.73 eV). This indicates that F—TiO$_2$ exhibits more pronounced n-type characteristics than pristine TiO$_2$. To understand the nature of charge extraction between the ETLs and perovskite, we investigated the charge extraction barrier (ΔE_e), which is the energy difference between the LUMOs of the ETLs and perovskite at the interface of the TiO$_2$/SnO$_2$ and SnO$_2$/perovskite, respectively. The ΔE_e of the SnO$_2$/perovskite did not change after F doping (backside F coating). Interestingly, F-TiO$_2$ had a smaller ΔE_e at the TiO$_2$/SnO$_2$ interface (0.09 eV) than pristine TiO$_2$ (–0.12 eV). A smaller ΔE_e indicates higher charge extraction efficiency. This implies that the charge extraction at the interface of F-TiO$_2$/SnO$_2$/perovskite is more efficient than that at the interface of TiO$_2$/SnO$_2$/perovskite.[46] Moreover, the better match in LUMO energy between F-TiO$_2$, SnO$_2$, and perovskite allowed efficient charge transfer into F-TiO$_2$ (Figure 3a).[47,48]

Figure 3b,c and **Table 3** show the results of the Hall effect measurements on F—TiO$_2$ as a function of the F-plasma time (F coating thickness parameters converted to F-plasma treatment time parameters). It is evident that the carrier concentration (n_{bulk}) decreased remarkably when TiO$_2$ was doped with F. The carrier concentration was primarily attributed to the V_O of TiO$_2$. Two free electrons were generated by each V_O defect site according to the V_O reaction (Equation 2):

$$O_O^x \rightarrow \frac{1}{2}O_2(g) + \ddot{V}_O + 2e \quad (2)$$

XPS analysis of the spectra in Figure 2c,d reveals that the generation of V_O in F-TiO$_2$ was suppressed upon F doping, because of which the number of carriers also decreased. The carrier concentration and electron mobility (μ_{hall}) are related by Equation 3,

$$\mu_{hall} = \frac{1}{\rho e n_{bulk}} \quad (3)$$

where μ_{hall} is the electron mobility, ρ is the resistivity, and e is the electronic charge (1.6×10^{-19} C) of the F-TiO$_2$ layer.

The electron mobility of F-TiO$_2$ is inversely proportional to the carrier concentration. Figure 3c shows that the electron mobility of TiO$_2$ reached a maximum of 61.3 cm^2 V^{-1} s^{-1} at an F-plasma time of 37.5 min, corresponding to 45% increase relative to the initial value (42.2 cm^2 V^{-1} s^{-1}). The increased electron
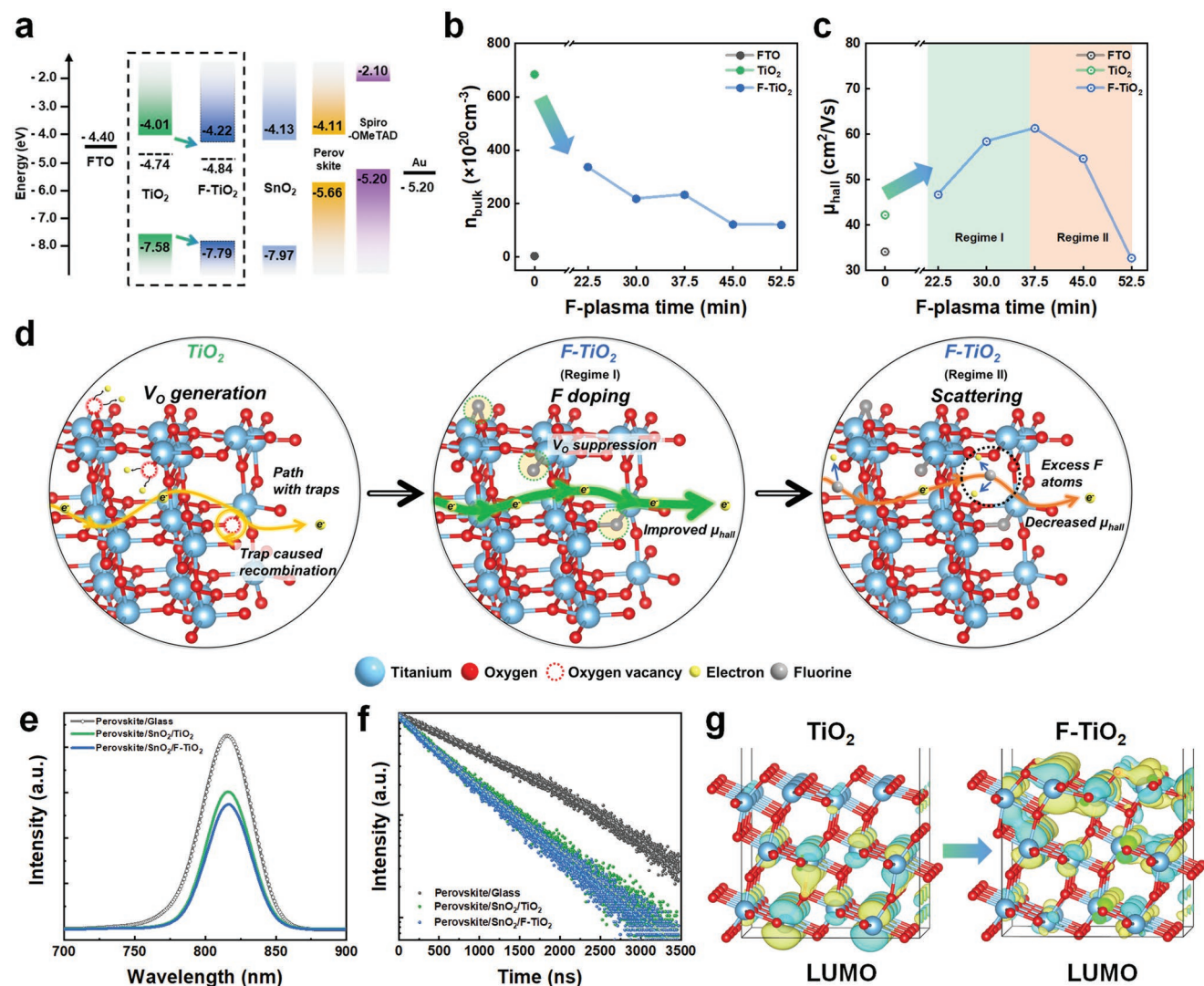
Figure 3. Enhanced charge transport properties of F-TiO$_2$ layer. a) Energy levels of the PSCs. b) Carrier concentration (n_{bulk}) and c) carrier mobility (μ_{hall}) of the TiO$_2$ and F-TiO$_2$ layer at various F-plasma times. d) F-TiO$_2$ structure with improved electron mobility. e) Steady-state PL spectra and f) corresponding TR-PL spectra of the perovskite film and perovskite film/SnO$_2$/TiO$_2$/FTO system with and without F doping. g) Electron density distribution for the LUMO level of the TiO$_2$ and F-TiO$_2$.

mobility enabled faster transport of the photogenerated electrons to the electrode (Regime I). When the F-plasma time was longer than 45 min, the electron mobility gradually decreased because of the enhanced scattering with an increasing number

Table 3. Hall effect measurement data of F-TiO$_2$ at different F-plasma times.

		Bulk concentration [n_{bulk}, × 10^{20} cm^{-3}]	Resistivity [ρ, × 10^{-5} Ω cm]	Mobility [μ_{hall}, cm^2 Vs^{-1}]
FTO		360	51.0	34.1
TiO$_2$		684	1.52	42.2
F-TiO$_2$	22.5 min	337	1.50	46.7
	30 min	218	1.47	58.4
	37.5 min	233	1.50	61.3
	45 min	122	1.49	54.6
	52.5 min	120	1.50	32.7

of F atoms (Regime II).[49,50] The change in electron mobility, as shown in Figure 3d, can be explained as follows. The V_O present in conventional TiO$_2$ limits the transport and collection of the photogenerated carriers. The initial increase in electron mobility in Regime I is attributed to the decrease in V_O, whereas the decrease in electron mobility in Regime II is a result of scattering by the excess F atoms. Figure S9 (Supporting Information) shows the scanning electron microscopy (SEM) and AFM images of TiO$_2$ and F-TiO$_2$. Although the TiO$_2$ surface has a rough surface, the F−TiO$_2$ surface becomes smooth upon the incorporation of F atoms, which can reduce the contact resistance.[51] As a result, the electron trap sites are eliminated, and the recombination is low.[52]

Figure 3e shows the steady-state photoluminescence (PL) spectra of perovskites coated on different samples. Compared to the control sample, significant PL quenching was observed for the perovskite on SnO$_2$/F-TiO$_2$, which was attributed to the higher electron mobility. Time-resolved photoluminescence

(TR-PL) spectra were recorded to further study the carrier transport dynamics at the interface between the perovskite and SnO_2/TiO_2 and were fitted by a bi-exponential decay function (Figure 3f). The fast decay component (τ_1) originates from the radiative recombination of free charge carriers in the bulk, while the slow decay component (τ_2) is attributed to charge-carrier quenching at the interface. The fitted values are listed in Table S4 (Supporting Information). The PL decay of the perovskite on $SnO_2/F\text{-}TiO_2$ was significantly faster than that on SnO_2/TiO_2, suggesting that the electron transfer from the perovskite to the former $SnO_2/F\text{-}TiO_2$ is more efficient than that to the latter.[46,53,54]

Indeed, the computational results using density functional theory calculations show that electron transfer can be improved as discussed below. Figure 3g shows the wavefunction of the LUMO overlaid on top of atomic structures of the TiO_2 and $F\text{-}TiO_2$ anatase models, which indicates that F doping contrib-

utes to delocalization in the LUMO. In a surface model with a doping ratio of 12.5%, LUMO is remarkably delocalized around F atoms, while this pattern is not clearly observed in the pure (101) surface. Noting that the electron population around the LUMO does not differ much between the two models (Figure S10, Supporting Information), it is possibly safe to conclude that F doping enhances the electron transport behavior in $F\text{-}TiO_2$.

2.4. Performance of F Coating and Doping Perovskite Solar Cells (F-PSC)

Conventional PSCs with a structure of glass/FTO/TiO_2/SnO_2/perovskite/octyl ammonium iodide (OAI)/$N2,N2,N2,N2,N7',N7',N7',N7$-octakis(4-methoxyphenyl)-9,9-spirobi[9H-fluorene]-2,2,7,7-tetramine (Spiro-OMeTAD)/Au (**Figure 4**a) were fabricated. Figure 4b shows the cross-sectional
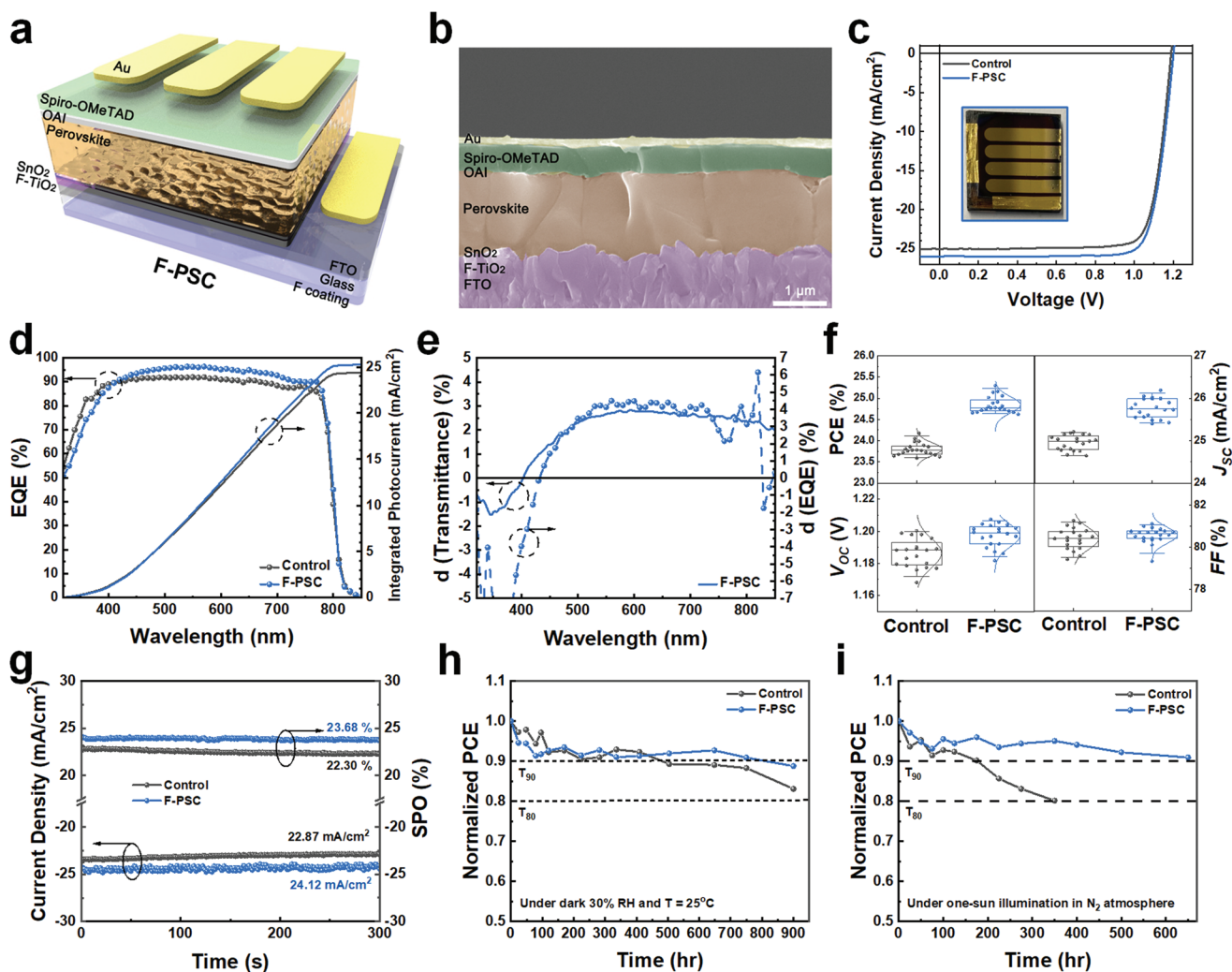

Figure 4. Performance of the PSCs with or without the F coating and F doping process (F-process). a) Schematic of the F-PSC. b) Cross-sectional SEM images of the F-PSC. c) J–V curves of the representative devices with or without 120 nm-thick F coating (inset shows an image of the F-PSC). d) EQE curves and the corresponding integrated photocurrent density curves of the solar cells. e) Differences in the transmittances and EQEs of devices with and without 120 nm-thick F coating. f) PCE, J_{SC}, V_{OC}, and FF distribution histogram of the control PSC and the F-PSC. g) Steady-state power/photocurrent output (SPO) tracking for the control and the F-PSC at the maximum power point. h) Air stability for unencapsulated control PSCs and F-PSCs. i) Long-term stability performance of the control PSC and F-PSCs under combined full-spectrum light in N_2 atmosphere.

**ADVANCED
SCIENCE NEWS**

www.advancedsciencenews.com

**ADVANCED
FUNCTIONAL
MATERIALS**

www.afm-journal.de

Table 4. Solar parameters of representative photovoltaic cells with or without F-process.

	J_{SC} [mA cm^{-2}]	Calc. J_{SC} [mA cm^{-2}]	V_{OC} [V]	FF [%]	PCE [%]
Control	25.05	24.37	1.189	81.15	24.17
	(25.00 ± 0.16)		(1.186 ± 0.009)	(80.46 ± 0.52)	(23.86 ± 0.13)
F-PSC	26.01	24.98	1.205	79.98	25.07
(F coating 90 nm)	(25.57 ± 0.34)		(1.189 ± 0.010)	(79.71 ± 1.34)	(24.23 ± 0.48)
F-PSC	26.01	25.23	1.202	80.93	25.30
(F coating 120 nm)	(25.79 ± 0.22)		(1.200 ± 0.006)	(80.49 ± 0.39)	(24.91 ± 0.18)
F-PSC	26.15	25.31	1.204	80.09	25.21
(F coating 150 nm)	(25.50 ± 0.42)		(1.189 ± 0.006)	(79.97 ± 1.40)	(24.26 ± 0.52)
F-PSC	25.86	25.08	1.203	81.29	25.29
(F coating 180 nm)	(25.40 ± 0.32)		(1.191 ± 0.008)	(80.83 ± 1.25)	(24.39 ± 0.52)
F-PSC	25.78	24.66	1.200	80.83	25.01
(F coating 210 nm)	(25.31 ± 0.32)		(1.186 ± 0.010)	(79.72 ± 1.65)	(23.93 ± 0.57)

SEM image of the F-PSC. The F-plasma coating process was employed to improve the efficiency of the PSCs (Figure 4c and **Table 4**). The bandgap of the perovskite is not changed after F coating (Figure S11, Supporting Information). In particular, J_{SC} improved upon F coating and F doping (designated as the F-process). These processes enhanced the transmittance of glass/FTO/TiO$_2$ and the electron mobility of TiO$_2$, thereby improving the photocurrent in the PSCs (Figure 1e; Figure S2, Supporting Information). F-PSC devices demonstrated significantly improved PCEs, with a maximum PCE of 25.30% (reverse scan, J_{SC} = 26.01 mA cm^{-2}, open-circuit voltage (V_{OC}) = 1.202 V, and fill factor (FF) = 80.93%). This corresponds to an absolute PCE gain of ≈1% upon the F-process. The hysteresis indices were 0.050 and 0.056 for PSC and F-PSC, respectively (Figure S12 and Table S5, Supporting Information), indicating that the F-process did not affect hysteresis.

The enhanced photocurrent of the PSCs after the F-process was also verified by measuring the external quantum efficiency (EQE) of the PSCs with and without the F-process (Figure 4d). The EQE of the F-PSC increased over a broad range of visible light. To elucidate the enhanced photocurrent after the F-process, we compared the difference between the transmittances of the glass/FTO/TiO$_2$ substrates (d(Transmittance)) and the difference between the EQEs of the control device and F-PSC (d(EQE)) (Figure 4e). Comparison reveals that the d(EQE) is proportional to d(Transmittance), indicating that the enhanced photocurrent results from the F-process, and this tends to increase for all F coating thicknesses (Figure S13, Supporting Information). As shown in the UV–vis absorption spectra (Figure S14, Supporting Information), light absorption intensity of the perovskite film with F-process was enhanced. The integrated photocurrents of the control device and F-PSC were calculated to be 24.37 and 25.23 mA cm^{-2}, respectively, which are close to the J_{SC} values obtained from the J–V measurements. The same results were obtained when devices with different thicknesses of the F coating were considered (Figure S15a—b, Supporting Information). The reproducibility was evaluated by statistical analysis. The photovoltaic parameters of 20 corresponding devices indicated that the performance of the F-PSC was more reproducible compared to that of the control device (Figure 4f). Figure S15c—f (Supporting Information) shows the reproducibility of the F-PSC with different F coating thicknesses.

The PCE and photocurrent output at the maximum power point (MPP) of the devices (initial PCE$_{Control}$ = 23.04%, PCE$_{F-PSC}$ = 24.10%) were continuously measured under simulated standard sunlight (AM 1.5G) (Figure 4g). The PCE of the control devices and F-PSCs finally stabilized at 22.30 and 23.68%, and the photocurrent density at 22.87 and 24.12 mA cm^{-2}, respectively. We studied the long-term stability of the PSCs at 30% RH for 900 h without encapsulation. The PCE of the F-PSC is stable at ≈89% of its original value while the control device shows ≈83% of its original PCE (Figure 4h). The enhanced environmental stability can be attributed to the hydrophobicity of the F-PSC compared to the control, which could be verified by WCA measurement of the F coating surface (Figure S16, Supporting Information).[55] In Figure 4i, we measured the stability of the control device and the F-PSC under full-spectrum light (100 mW cm^{-2}) in N$_2$ atmosphere. The PCE of the control device retains ≈80% after 350 h, while the PCE of the F-PSC retains ≈91% of its initial value for 650 h. Thus, the result elucidates that the F-TiO$_2$ has a positive effect on the long-term stability.

3. Conclusion

In conclusion, we have demonstrated that inclined F sputtering can implement an AR effect by virtue of F coating and F doping on the TiO$_2$ ETL in PSCs. In this sputtering process, the average transmittance of the F-coated FTO/TiO$_2$ increases significantly because of the very low refractive index of the F coating. Depositing an AR F coating is an effective method for reducing the up to 39.4% reflection loss caused by FTO and TiO$_2$. In addition, the inclined sputtering method allows F to be doped on the backside of the TiO$_2$ surface, which effectively suppresses oxygen vacancies in TiO$_2$ and enhances electron mobility. Under the combined effects of F coating and F doping, J_{SC} of the F-PSC increases from 25.05 to 26.01 mA cm^{-2}, and the PCE increases from 24.17% to 25.30%. Regarding stability, the F-PSC exhibits enhancement in ambient air, retaining >90% of its initial PCE after 900 h under 30% RH condition. Likewise, the F-PSC exhibits a significant improvement in light stability under one-sun illumination in N$_2$ atmosphere, with ≈91% of its initial efficiency retained after 650 h. This work demonstrates

that the inclined F sputtering technology is a simple and effective method to increase J_{SC} of PSCs through the improved transmittance of FTO/TiO$_2$ and electrical characteristics of the ETLs.

4. Experimental Section

Fabrication of Sputtering Target and the F-Plasma Process: The CNT–PFA composite targets for sputtering were cut into disks with a diameter and thickness of 10.16 cm and 6 mm, respectively.[55] FTO glass (thickness: 650 nm, 15 mm × 15 mm, 2.2T, TEC7, Pilkington) was cleaned ultrasonically in deionized water, acetone, and 2-propanol for 10 min each. To fabricate the TiO$_2$ layer, 60 mL of a titanium diisopropoxide bis(acetylacetonate)/ethanol (1:10) solution was sprayed using a spray gun at 450 °C under an oxygen atmosphere. After the TiO$_2$ layer (thickness: 20 nm) was fabricated, the substrates were stored at 450 °C for 1 h. The F coating on FTO glass/ TiO$_2$ was fabricated using a power source with an MF (PE II, Advanced Energy) of 40 kHz and a sputtering power density of 1.85 W cm^{-2}. The sputtering chamber was evacuated to a high vacuum level of 3.0×10^{-6} Torr using a mechanical rotary pump and cryopump. The working pressure of argon gas was 8 mTorr, which was maintained using a mass flow controller. The target-to-substrate distance was maintained at 240 mm.[56] To ensure a uniform F coating, the cathode head was inclined by ≈10°. The thicknesses of the F coatings were measured using a profilometer (α-step 250, Tencor). F coatings with thicknesses of 90, 120, 150, 180, and 210 nm were deposited by adjusting the coating time to 22.5, 30, 37.5, 45, and 52.5 min, respectively.

Characterization of F Coating and F-TiO$_2$ ETL: The refractive indices of FTO, TiO$_2$, and the F coating were determined by SE (Elli-SE, Ellipso Technology; Figure S17, Supporting Information). After storing the complex refractive indices of the materials in the Essential Macleod program software (Thin Film Center), the optical properties were simulated according to the wavelength (Table S6, Supporting Information). Optical transmittance and reflectance were measured in the wavelength range of 300–1200 nm using an optical spectrometer (U-4100, Hitachi). The sheet resistances of the samples were measured at room temperature using a standard four-point probe technique (MCP-T610, Mitsubishi Chemical Analytech). The structure and elemental composition of the layers were investigated by field-emission TEM (JEM-ARM200F, JEOL). The specimens were prepared using a focused ion beam. The surface morphology was investigated by field-emission SEM (SEM, MAIA3, TESCAN) and AFM (XE-100, Park Systems). The AFM instrument was operated in the tapping mode with a scan range of 2 μm × 2 μm.

The chemical structure was determined by XPS (AXIS NOVA, Kratos). The XPS measurement vacuum degree was 10^{-9} Torr, and the characteristic X-ray was Al-Kα (1486.6 eV). X-rays were generated by applying an electric field with an acceleration voltage of 15 keV and acceleration current of 10 mA. Depth profiling was performed by TOF-SIMS (ION-TOF M6, Germany) using a sputtering beam of O$_2^+$ at 1 keV with a raster size of 500 μm × 500 μm and an analysis beam of Bi^{3+} at 30 keV with a raster size of 100 μm × 100 μm. High-resolution XRD patterns were obtained using a high-power diffractometer (D/MAX2500V/PC, Rigaku) at a potential of 40 kV and current of 200 mA with a Cu-rotating anode and Cu Kα radiation ($\lambda = 0.1542$ nm) using a graphite monochromator and scintillation counter. The WCA was measured using a contact angle tester (Phoenix 300 Touch, Surface Electro Optics) with 5 μL of deionized (DI) water.

The UPS measurements were conducted using ESCALAB 250XI. The electrical properties were measured using a Hall effect measurement system (HMS-7000, Ecopia) at a magnetic field of 0.543 T and operating current of 0.001 mA. The UV–vis–near-infrared absorption spectra were obtained on a Cary 5000 (Agilent) spectrophotometer, and the PL spectra were obtained on an nF900 instrument (Edinburgh Photonics) using a xenon lamp as the excitation source. The TR-PL measurements

were conducted using a PicoQuant FluoTime 300 (PicoQuant GmbH, Germany) instrument equipped with a PDL 820 laser pulse driver. A pulsed laser diode ($\lambda = 375$ nm, pulse FWHM < 70 ps, repetition rate 200 kHz-40 MHz) was used to excite the samples. The PL lifetime was determined using a commercial software (Origin 2020), and the TR-PL data were fitted to a two-exponential decay function (Equation 4).

$$y = y_0 + A_1 e^{-x/\tau_1} + A_2 e^{-x/\tau_2} \tag{4}$$

where A_1, A_2, τ_1, and τ_2 are the amplitudes and lifetimes of the exponential components, respectively.

To investigate the electronic structures of the TiO$_2$ anatase surface and the effect of F doping, the projector-augmented wave (PAW) method implemented in the Vienna ab initio Simulation Package (VASP) was adopted.[57] Starting with the pure anatase TiO$_2$ structure with lattice parameters a = 3.802 Å and c = 9.748), the TiO$_2$ (101) surface was simulated using a (2 × 3) periodic slab model (108 atoms) separated by a 15 Å thick vacuum region. To determine the surface doping effect, one surface O atom was replaced by an F atom, analogous to the F-doping ratio of 12.5%. Geometry optimization of the surface models was conducted with a convergence criterion of 10^{-6} eV Å^{-1}, where the top two layers were fully relaxed, while the bottom layer was fixed to represent the bulk region. A Monkhorst-Pack mesh of k-points (2 × 2 × 1 points) was used to sample the Brillouin zone with a cutoff energy of 520 eV and self-consistent energy convergence tolerance of 10^{-6} eV. To accurately predict the electronic structures of the transition metal oxides,[58] the Heyd-Scuseria-Ernzerhof (HSE06)[59,60] hybrid density functional was adopted.

Fabrication of F-PSC: SnO$_2$ colloidal solution was purchased from Alfa Aesar. Titanium diisopropoxide bis(acetylacetonate), ethylenediaminetetraacetic acid (EDTA, 99%), *N*,*N*-dimethylformamide (DMF, anhydrous, 99.8%), dimethyl sulfoxide (DMSO, 99.9%), cesium iodide (CsI, 99.9%), methylamine hydrochloride (MACl, 98%), 2-propanol (IPA, anhydrous, 99.5%), chlorobenzene (CB anhydrous, 99.8%), acetonitrile (ACN, 99.8%), 4-tert-butylpyridine (tBP), and Li-bis(trifluoromethanesulfonyl)imide (Li-TFSI, 99.95%) were purchased from Sigma–Aldrich. FK209 Co(III)-TFSI salt was purchased from Lumtec. Formamidinium iodide (FAI, 99.99%), methylammonium bromide (MABr, 99.99%), and octylammonium iodide (OAI, 99%) were purchased from GreatCell Solar. Ethyl ether (DEE 99.5%) was purchased from Samchun. Lead iodide (PbI$_2$, 99.99%) and lead bromide (PbBr$_2$, 98%) were purchased from TCI.

To fabricate a thin EDTA-SnO$_2$ layer, SnO$_2$ (from Alfa Aesar) was diluted 20 folds with DI water and mixed with EDTA (0.2 mg mL^{-1}) under overnight stirring at 80 °C.[46] The TiO$_2$-coated substrates were subjected to UVO treatment for 30 min. The resulting solution was spin-coated onto the pretreated TiO$_2$ layer at 4000 rpm for 30 s. The substrates were then heated to 150 °C for 20 min.

The perovskite precursor solution was prepared by dissolving 245 mg FAI, 1.29 mg MABr, 15.6 mg CsI, 748 mg PbI$_2$, 4.40 mg PbBr$_2$, and 35.4 mg MACl in a 1 mL DMF/DMSO (8:1) solution. The perovskite solution was filtered through a PTFE filter (0.2 μm). After the UVO treatment, the filtered perovskite precursor solution was spin-coated in sequential steps. The first step was 1000 rpm for 10 s with an acceleration of 2000 rpm·s. The second step was 4000 rpm for 35 s with an acceleration of 1500 rpm·s. During the second spin-coating step, 1 mL of diethyl ether was added dropwise onto the substrates 20 s before the completion of spin coating. The perovskite films were then transferred onto a hotplate and annealed at 100 °C for 60 min. After cooling the substrates, 15 mM of OAI solution dissolved in 2-propanol was spin-coated on the perovskite layer at 3000 rpm for 30 s. For the hole-transport layer, the spiro-OMeTAD solution was spin-coated onto the perovskite layer at 3000 rpm for 30 s. Spiro-OMeTAD (90 mg/mL in CB) was doped with 39 μL tBP, 23 μL Li-TFSI (520 mg mL^{-1} in ACN), and 10 μL Co-TFSI (300 mg mL^{-1} in ACN). The devices were pumped under vacuum (< 10^{-6} Torr), and an 80 nm-thick Au electrode was deposited by thermal evaporation. Based on the deposited Au electrode area, the active area of the device was 10.5 mm^2.

Characterization of Device Performances and Stability: The solar cell performance was determined using a Keithley 2635A source measurement. A high-quality optical fiber was used to guide the light from a solar simulator to the device under AM 1.5G illumination at 100 mW cm^{-2}. The *J*–*V* curves were obtained with a scanning rate of voltage interval 20 mV and delay time 40 ms from 1.30 to -0.01 V (reverse) or from −0.01 to 1.30 V (forward). EQEs of the PSCs were measured using a QEX7 system (PV Measurement, Inc.).

The air stability measurements of the unencapsulated control devices and F-PSCs were performed at 30% RH and 25 °C under dark condition. The PCEs of the devices were periodically obtained under AM 1.5G simulated sunlight illumination in an N$_2$ glove box. The light stability of the devices was measured under a full-spectrum Xenon lamp in N$_2$ atmosphere. A UV filter was not used during the aging process. For *J*–*V* characterization, the devices were taken out of the aging chamber, cooled, and tested.

Supporting Information

Supporting Information is available from the Wiley Online Library or from the author.

Acknowledgements

Conflict of Interest

The authors declare no conflict of interest.

Data Availability Statement

The data that support the findings of this study are available from the corresponding author upon reasonable request.

Keywords

[1] Z. Chen, Q. Dong, Y. Liu, C. Bao, Y. Fang, Y. Lin, S. Tang, Q. Wang, X. Xiao, Y. Bai, Y. Deng, J. Huang, *Nat. Commun.* **2017**, *8*, 1890.

[2] Q. Dong, Y. Fang, Y. Shao, P. Mulligan, J. Qiu, L. Cao, J. Huang, *Science* **2015**, *347*, 967.

[3] M. Baranowski, P. Plochocka, *Adv. Energy Mater.* **2020**, *10*, 1903659.

[4] S. Tao, I. Schmidt, G. Brocks, J. Jiang, I. Tranca, K. Meerholz, S. Olthof, *Nat. Commun.* **2019**, *10*, 2560.

[5] S. Sánchez, S. Cacovich, G. Vidon, J.-F. Guillemoles, F. Eickemeyer, S. M. Zakeeruddin, J. E. K. Schawe, J. F. Löffler, C. Cayron, P. Schouwink, M. Gräetzel, *Energy Environ. Sci.* **2022**, *15*, 3862.

[6] S. Hu, K. Otsuka, R. Murdey, T. Nakamura, M. A. Truong, T. Yamada, T. Handa, K. Matsuda, K. Nakano, A. Sato, K. Marumoto, K. Tajima, Y. Kanemitsu, A. Wakamiya, *Energy Environ. Sci.* **2022**, *15*, 2096.

[7] J. Y. Kim, J.-W. Lee, H. S. Jung, H. Shin, N.-G. Park, *Chem. Rev.* **2020**, *120*, 7867.

[8] J. Seo, J. H. Noh, S. I. Seok, *Acc. Chem. Res.* **2016**, *49*, 562.

[9] National Renewable Energy Laboratory, Best Research-Cell Efficiency Chart, https://www.nrel.gov/pv/cell-efficiency.html (accessed: December 2022).

[10] A. Kojima, K. Teshima, Y. Shirai, T. Miyasaka, *J. Am. Chem. Soc.* **2009**, *131*, 6050.

[11] A. Krishna, H. Zhang, Z. Zhou, T. Gallet, M. Dankl, O. Ouellette, F. T. Eickemeyer, F. Fu, S. Sanchez, M. Mensi, S. M. Zakeeruddin, U. Rothlisberger, G. N. M. Reddy, A. Redinger, M. Grätzel, A. Hagfeldt, *Energy Environ. Sci.* **2021**, *14*, 5552.

[12] E. L. Lim, A. Hagfeldt, D. Bi, *Energy Environ. Sci.* **2021**, *14*, 3256.

[13] J. Jeong, M. Kim, J. Seo, H. Lu, P. Ahlawat, A. Mishra, Y. Yang, M. A. Hope, F. T. Eickemeyer, M. Kim, Y. J. Yoon, I. W. Choi, B. P. Darwich, S. J. Choi, Y. Jo, J. H. Lee, B. Walker, S. M. Zakeeruddin, L. Emsley, U. Rothlisberger, A. Hagfeldt, D. S. Kim, M. Grätzel, J. Y. Kim, *Nature* **2021**, *592*, 381.

[14] M. Kim, I.-W. Choi, S. J. Choi, J. W. Song, S.-I. Mo, J.-H. An, Y. Jo, S. Ahn, S. K. Ahn, G.-H. Kim, D. S. Kim, *Joule* **2021**, *5*, 659.

[15] H. Min, D. Y. Lee, J. Kim, G. Kim, K. S. Lee, J. Kim, M. J. Paik, Y. K. Kim, K. S. Kim, M. G. Kim, T. J. Shin, S. I. Seok, *Nature* **2021**, *598*, 444.

[16] M. Kim, J. Jeong, H. Lu, T. K. Lee, F. T. Eickemeyer, Y. Liu, I. W. Choi, S. J. Choi, Y. Jo, H.-B. Kim, S.-I. Mo, Y.-K. Kim, H. Lee, N. G. An, S. Cho, W. R. Tress, S. M. Zakeeruddin, A. Hagfeldt, J. Y. Kim, M. Grätzel, D. S. Kim, *Science* **2022**, *375*, 302.

[17] J. J. Yoo, S. S. Shin, J. Seo, *ACS Energy Lett.* **2022**, *7*, 2084.

[18] N.-G. Park, M. Grätzel, T. Miyasaka, K. Zhu, K. Emery, *Nat. Energy* **2016**, *1*, 16152.

[19] F. Berry, R. Mermet-Lyaudoz, J. M. C. Davila, D. A. Djemmah, H. S. Nguyen, C. Seassal, E. Fourmond, C. Chevalier, M. Amara, E. Drouard, *Adv. Energy Mater.* **2022**, *12*, 2200505.

[20] H. Li, C. Chen, H. Hu, Y. Li, Z. Shen, F. Li, Y. Liu, R. Liu, J. Chen, C. Dong, S. Mabrouk, R. S. Bobba, A. Baniya, M. Wang, Q. Qiao, *InfoMat* **2022**, *4*, e12322.

[21] G. Sathiyan, H. Wang, C. Chen, Y. Miao, M. Zhai, M. Cheng, *Dyes Pigm.* **2022**, *198*, 110029.

[22] N. A. N. Ouedraogo, H. Yan, C. B. Han, Y. Zhang, *Small* **2021**, *17*, 2004081.

[23] X. Wang, K. Rakstys, K. Jack, H. Jin, J. Lai, H. Li, C. S. K. Ranasinghe, J. Saghaei, G. Zhang, P. L. Burn, I. R. Gentle, P. E. Shaw, *Nat. Commun.* **2021**, *12*, 52.

[24] J. Yang, C. Liu, C. Cai, X. Hu, Z. Huang, X. Duan, X. Meng, Z. Yuan, L. Tan, Y. Chem, *Adv. Energy Mater.* **2019**, *9*, 1900198.

[25] T. Okazoe, *Proc Jpn Acad* **2009**, *85*, 276.

[26] J. R. de Laeter, J. K. Böhlke, P. de Bièvre, H. Hidaka, H. S. Peiser, K. J. R. Rosman, P. D. P. Taylor, *Pure Appl. Chem.* **2003**, *75*, 683.

[27] J. Emsley, *The Elements*, Oxford University Press, Oxford, UK **1998**.

[28] C. M. Sharts, *J. Chem. Educ.* **1968**, *45*, 185.

[29] Q. Zhang, M. A. Kelly, N. Bauer, W. You, *Acc. Chem. Res.* **2017**, *50*, 2401.

[30] T. L. Nguyen, H. Choi, S.-J. Ko, M. A. Uddin, B. Walker, S. Yum, J.-E. Jeong, M. H. Yun, T. J. Shin, S. Hwang, J. Y. Kim, H. Y. Woo, *Energy Environ. Sci.* **2014**, *7*, 3040.

[31] F. Babudri, G. M. Farinola, F. Naso, R. Ragni, *Chem. Commun.* **2007**, *10*, 1003.

[32] X. Zhu, M. Du, J. Feng, H. Wang, Z. Xu, L. Wang, S. Zuo, C. Wang, Z. Wang, C. Zhang, X. Ren, S. Priya, D. Yang, S. Liu, *Angew. Chem., Int. Ed.* **2021**, *60*, 4238.

[33] Q. Zhu, J. Wu, P. Yuan, M. Zhang, Y. Dou, X. Wang, J. Zou, W. Sun, L. Fan, Z. Lan, *Energy Technol.* **2020**, *8*, 1901017.

[34] G. Y. Yoo, N. Nurrosyid, S. Lee, Y. Jeong, I. Yoon, C. Kim, W. Kim, S.-Y. Jang, Y. R. Do, *ACS Appl. Mater. Interfaces* **2020**, *12*, 10626.

[35] W. Groh, A. Zimmermann, *Macromolecules* **1991**, *24*, 6660.

[36] H. K. Park, S. W. Yoon, W. W. Chung, B. K. Min, Y. R. Do, *J. Mater. Chem. A* **2013**, *1*, 5860.

[37] G. Haacke, *J. Appl. Phys.* **1976**, *47*, 4086.

[38] D. A. Jacobs, K. R. Catchpole, F. J. Beck, T. P. White, *J. Mater. Chem. A* **2016**, *4*, 4490.

[39] X. Zhang, Y. Wu, Y. Huang, Z. Zhou, S. Shen, *J. Alloys Compd.* **2016**, *681*, 191.

[40] W. Zhao, H. Li, Z. Liu, D. Wang, S. Liu, *Sol. Energy Mater. Sol. Cells* **2018**, *182*, 263.

[41] C. Y. Neo, J. Ouyang, *J. Power Sources* **2013**, *241*, 647.

[42] A. Ghobadi, T. Ulusoy, R. Garifullin, M. O. Guler, A. K. Okyay, *Sci. Rep.* **2016**, *6*, 30587.

[43] T. G. Ulusoy, A. Ghobadi, A. K. Okyay, *J. Mater. Chem. A* **2014**, *2*, 16867.

[44] M. Z. Toe, S. Y. Pung, K. A. Yaacob, A. Matsuda, W. K. Tan, S. S. Han, *J. Sol-Gel Sci. Technol.* **2020**, *95*, 439.

[45] E. Elangovan, K. Ramamurthi, *Thin Solid Films* **2005**, *476*, 231.

[46] J. Tao, X. Liu, J. Shen, H. Wang, J. Xue, C. Su, H. Guo, G. Fu, S. Kong, S. Yang, *Chem. Eng. J.* **2022**, *430*, 132683.

[47] H. Tan, A. Jain, O. Voznyy, X. Lan, F. P. G. de Arquer, J. Z. Fan, R. Quintero-Bermudez, M. Yuan, B. Zhang, Y. Zhao, F. Fan, P. Li, L. N. Quan, Y. Zhao, Z.-H. Lu, Z. Yang, S. Hoogland, E. H. Sargent, *Science* **2017**, *355*, 722.

[48] J. P. C. Baena, L. Steier, W. Tress, M. Saliba, S. Neutzner, T. Matsui, F. Giordano, T. J. Jacobsson, A. R. S. Kandada, S. M. Zakeeruddin, A. Petrozza, A. Abate, M. K. Nazeeruddin, M. Grätzel, A. Hagfeldt, *Energy Environ. Sci.* **2015**, *8*, 2928.

[49] A. Reed, C. Stone, K. Roh, H. W. Song, X. Wang, M. Y. Liu, D.-K. Ko, K. No, S. Lee, *J. Mater. Chem. C* **2020**, *8*, 13798.

[50] S. Lan, S. Yoon, H.-J. Seok, H. U. Ha, D.-W. Kang, H.-K. Kim, *ACS Appl. Energy Mater.* **2022**, *5*, 234.

[51] J. Y. Kim, S. Rhee, H. Lee, K. An, S. Biswas, Y. Lee, J. W. Shim, C. Lee, H. Kim, *Adv. Mater. Interfaces* **2020**, *7*, 1902003.

[52] T. Wu, R. Zhuang, R. Zhao, R. Zhao, L. Zhu, G. Liu, R. Wang, K. Zhao, Y. Hua, *ACS Energy Lett.* **2021**, *6*, 2218.

[53] D. Yang, R. Yang, K. Wang, C. Wu, X. Zhu, J. Feng, X. Ren, G. Fang, S. Priya, S. Liu, *Nat. Commun.* **2018**, *9*, 3239.

[54] J. Tao, N. Ali, K. Chen, Z. Huai, Y. Sun, G. Fu, W. Kong, S. Yang, *J Mater Chem* **2019**, *7*, 1349.

[55] E. Cho, Y. Y. Kim, D. S. Ham, J. H. Lee, J.-S. Park, J. Seo, S.-J. Lee, *Nano Energy* **2021**, *82*, 105737.

[56] S. H. Kim, C. H. Kim, W. J. Choi, T. G. Lee, S. K. Cho, Y. S. Yang, J. H. Lee, S.-J. Lee, *Sci. Rep.* **2017**, *7*, 1451.

[57] G. Kresse, J. Furthmüller, *Comput. Mater. Sci.* **1996**, *6*, 15.

[58] J. Wang, J. Huang, J. Meng, Q. Li, J. Yang, *RSC Adv.* **2017**, *7*, 39877.

[59] J. Heyd, G. E. Scuseria, M. Ernzerhof, *J. Chem. Phys.* **2003**, *118*, 8207.

[60] J. Heyd, G. E. Scuseria, M. Ernzerhof, *J. Chem. Phys.* **2006**, *124*, 219906.

2301033 (11 of 11)